Ceramics International 51 (2025) 18073–18085

Contents lists available at ScienceDirect

Ceramics International

journal homepage: www.elsevier.com/locate/ceramint

Impact of synthesis methods and coordination agents on the structure, morphology, and luminescent efficiency of triple-doped Nd^{3+}, Yb^{3+} and Tm^{3+} yttrium orthovanadate

María Rapp [a,*], Elisa Ortiz-Rivero [b,c], Josefa Isasi [a,**], Mauricio Alcolea Palafox [d]

[a] Departamento de Química Inorgánica, Facultad de Ciencias Químicas, Universidad Complutense de Madrid, Ciudad Universitaria s/n, 28040, Madrid, Spain
[b] Nanomaterials for Bioimaging Group (nanoBIG), Departamento de Física de Materiales, Facultad de Ciencias & Instituto de materiales Nicolás Cabrera, Universidad Autónoma de Madrid, C/ Francisco Tomás y Valiente 7, 28049, Madrid, Spain
[c] Department of Physics, University of Gothenburg, 41296, Gothenburg, Sweden
[d] Departamento de Química Física, Facultad de Ciencias Químicas, Universidad Complutense de Madrid, Ciudad Universitaria s/n, 28040, Madrid, Spain

ARTICLE INFO

Handling Editor: Dr P. Vincenzini

Keywords:
Sol-gel and hydrothermal synthesis
Silica coated samples
Luminescence study
Down-shifting and up-conversion process

ABSTRACT

The research and study of novel fluorescent nanomaterials based on lanthanide ions that can be excited by infrared radiation is essential for the development of new technologies in the biomedicine, photonics, and optoelectronics fields. The present work focuses on the structural and morphological study of new orthovanadate $Y_{0.9}Nd_{0.02}Tm_{0.03}Yb_{0.05}VO_4$ and $Y_{0.9}Nd_{0.02}Tm_{0.05}Yb_{0.03}VO_4$ samples. Their optical properties were also analyzed, including the evaluation of up-conversion (UC) and down-conversion (DS) mechanisms under infrared excitation at 980 nm and 808 nm. The samples were synthesized using both the sol-gel method and hydrothermal synthesis with urea and citric acid (CA) or maleic acid (MA) addition. These samples were reacted with tetraethyl orthosilicate (TEOS) to obtain silica-coated samples. X-ray diffraction (XRD) analysis confirmed the tetragonal symmetry compatible with a zircon-type structure of the diffraction pattern. FTIR spectra revealed bands corresponding to the several vibrational modes of VO_4^{3-} groups and the presence of silica in the TEOS-treated samples. The synthesis method and the addition of CA or MA influenced the agglomeration, shape and morphology of the particles, as evidenced by transmission electron microscopy images. Photoluminescence (PL) studies of investigated samples after being excited with infrared radiation provided a detailed description of the energy transfer mechanisms involved in the DS and UC processes. These processes are related to the synthesis method used to obtain them and to the chelating agents added. Excitation of the samples at 808 nm generates DS processes and PL spectra with bright emission bands corresponding to electronic transitions of the Nd^{3+} and Yb^{3+} ions, while excitation at 808 and 980 nm gives rise to UC processes and PL spectra showing intense blue, red and NIR-I emission bands of Tm^{3+} ions, along with green and red emissions of Nd^{3+} ions.

1. Introduction

In recent decades, lanthanide (Ln^{3+}) doped nanomaterials samples with capacity to generate luminescence within the ultraviolet (UV)-visible and near infrared (NIR) spectrum range have been studied. Some of these samples have been investigated based on their potential application in bioimaging and biomedicine [1]. The use of these samples in phototherapy may represent the beginning of different alternatives to replace conventional invasive oncological treatments such as surgery, chemotherapy or radiotherapy. Therefore, the spectroscopic study of Ln-doped nanomaterial samples and their subsequent development and implementation constitutes a first step in the search for new therapy forms.

When investigating the process of obtaining Ln^{3+} doped samples, it is necessary to consider two fundamental parameters, which are the choice of the host network, and the dopant ions present in its composition. Non-optically active host lattices with low phonon energies should be used to minimize non-radiative energy losses [2]. The main function of the lattice will be to host dopant ions in low symmetry positions. For some time, we have been investigating the use of YVO_4 as a host matrix for

* Corresponding author.
** Corresponding author.
E-mail addresses: mrapp@ucm.es (M. Rapp), isasi@ucm.es (J. Isasi).

https://doi.org/10.1016/j.ceramint.2025.01.583
Received 10 December 2024; Received in revised form 28 January 2025; Accepted 30 January 2025
Available online 2 February 2025

lanthanide ions due to its high chemical and thermal stability, as well as its high transmittance in the visible range and low absorption of incident radiation, making it suitable for applications in optical devices and biomedicine.

In Ln-doped YVO_4 samples, the multiple energy levels present in the electronic structure of Ln^{3+} ions allow photoexcitation of its population using low-energy radiation such as NIR. This radiation has a high penetration capacity in living tissues, allowing the observation of Stokes and anti-Stokes phenomena [3–7].

The luminescence process based on the absorption of a single NIR photon, followed by the Stokes emission of a lower energy photon is known as down-shift (DS). In DS processes, the radiation emission can occur in the NIR range (750–1800 nm), which falls within the so-called biological transparency windows [8]. On the other hand, UC mechanisms involve the absorption of two or more low-energy incident photons by a sensitizing ion (usually Yb^{3+}) and the subsequent energy transfer (ET) to certain activating ions such as Er^{3+}, Tm^{3+} or Ho^{3+}. The transferred energy excites the electrons of the activator ions to high-energy excited states, resulting in anti-Stokes emission of high-energy radiation. The Yb^{3+} ion is commonly used as a sensitizer due to its ability to absorb NIR radiation, as its energy gap between the ground and excited states is 980 nm [6,9]. However, in studies carried out in biological media, it is found that water exhibits a high absorption of incident radiation at 980 nm, which reduces the emission intensity in samples doped with ytterbium upon excitation [1]. To avoid this limitation, an alternative may be to incorporate neodymium in the composition of samples of this type. These Nd^{3+} ions will act as sensitizing ions under photoexcitation at 808 nm. At this wavelength, the water absorption coefficient is significantly lower (0.02 cm^{-1}) compared to that resulting from photoexcitation at 980 nm (0.48 cm^{-1}), so this change in the composition of the samples allows to reduce the absorption of radiation by water molecules, improving an efficiency emission both *in vitro* and *in vivo* assays [9].

In the search for new Ln-doped YVO_4 samples, it is also important to consider parameters such as the size and shape of the particles present in the samples investigated. Numerous studies have shown that both the synthesis method and changes in reaction parameters directly influence the composition, morphology, and size of the prepared particles, thereby affecting their physical and chemical properties. The control of these parameters allows us to obtain nanomaterial samples with desired characteristics and properties for their final applications [10–12]. However, in most cases it has been found that the obtained samples present surface defects, which cause a decrease in the luminescence emission intensity. Core-shell structures with silica as a coating agent have been used to overcome the problem caused by surface defects or to make them more biocompatible, thus reducing their toxicity or delaying their immunological recognition [13–15]. Amorphous silica is one of the most used precursors for nanoparticle surface modification, as it reduces surface defects, is highly biocompatible and is transparent to electromagnetic radiation in the 300–800 nm range. The most well-known method for the formation of silica coatings is the Stöber method, which is a sol-gel derived process where TEOS is generally used as precursor of silica [13].

Based on the above considerations, this paper describes the synthesis and study of $Y_{0.9}Nd_{0.02}Tm_{0.03}Yb_{0.05}VO_4$ and $Y_{0.9}Nd_{0.02}Tm_{0.05}Yb_{0.03}VO_4$ samples, which were prepared by two soft chemistry methods, namely the sol-gel (SG) method and hydrothermal (HT) synthesis with urea addition which acts as a combustible agent, along with two chelating agents such as CA or MA. Silica-coated samples were also obtained by reaction of the previously synthesized ones with TEOS. The influence of the synthesis method and thulium and terbium content on structure, powder morphology and luminescent emission efficiency by DS and UC processes were investigated in detail. These samples incorporate Nd^{3+} ions as sensitizers in addition to Yb^{3+} ions in their composition, allowing the radiation absorption at 808 nm and reducing the absorption of this radiation by water present in a biological medium. On the other hand, the Tm^{3+} ions also present in the compositions at 0.02 and 0.05 % will act as activator ions that show high-energy and long-lived metastable excited states [6].

2. Experimental

For comparative purposes, two $Y_{0.9}Nd_{0.02}Tm_{0.03}Yb_{0.05}VO_4$ and $Y_{0.9}Nd_{0.02}Tm_{0.05}Yb_{0.03}VO_4$ samples were prepared by both sol-gel method and hydrothermal synthesis. Yttrium, thulium, neodymium and ytterbium nitrates [$(Y(NO_3)_3{\cdot}6H_2O$ (99.8 %, Strem Chemicals), $Tm(NO_3)_3{\cdot}5H_2O$ (99.9 %, Strem Chemicals), $Nd(NO_3)_3{\cdot}6H_2O$ (99.8 %, Sigma-Aldrich), $Yb(NO_3)_3 \cdot 6H_2O$ (99.8 %, Strem Chemicals)] as well as ammonium vanadate (NH_4VO_3, (≥99 %, Sigma Aldrich analytical grade) were used as starting precursors. Urea ($CO(NH_2)_2$) (PanReac, 99,0–100,5 %) was used as combustible agent. CA ($C_6H_8O_7$) (≥99 %, Sigma Aldrich) and MA ($C_4H_4O_4$) (Acrös Organics, 99 %) were used as chelating agents. Finally, ethylene glycol (EG) ($C_2H_6O_2$) (99 %, PanReac) was used as polymerizing agent.

CA is an organic ligand with three carboxylate groups and MA is a bidentate ligand consisting of two carboxylic acids that can form coordination complexes with Y^{3+} and Ln^{3+} ions. The formation of coordination complexes helps to control the nucleation process and the growth of the crystal nucleus [25]. However, in presence of other anions such as VO_4^{3-}, a competition for the cations coordinated to organic ligands appears, leading to $YLnVO_4$ seeds formation that will grow surrounded by citrate and malonate ions, limiting their fine size and obtaining samples with nanometric particle size and rounded morphology by favouring anisotropic growth.

2.1. Sol-gel synthesis

For the preparation of the two samples, 0.25 g of NH_4VO_3 and stoichiometric amounts of nitrate precursors were dissolved in two different beakers by adding 100 mL of deionized water. The resulting yellow solutions were heated to 100 °C under magnetic stirring for 30 min. Subsequently, CA was added in a 1:1 M ratio [16,17] regarding to the amount of NH_4VO_3 added.

The reactions were allowed to proceed for 30 min and during this time a new color change was observed from yellow to blue. This fact was indicative of the CA reaction with the metal cations involved in the respective compositions to form complexes. At this point, it should be noted that citric acid acts as a chelating agent giving rise to the corresponding citrates or metal complexes of the metal cations, which are much more soluble $[Y_{1-x-y-z}Nd_xTm_yYb_z(C_6H_8O_7)_3](NO_3)_3$ and $VO(C_6H_7O_7)_2$ [16,17] and avoids the secondary phases formation.

30 min later, urea was added in a 1:1 M ratio regarding the calculated amount of NH_4VO_3. Next, 2 mL of EG was added to introduce a viscous reaction medium. This reagent produces a cross-esterification of the above metal complexes, resulting in the formation of amorphous three-dimensional networks within these solutions [18].

Gels were formed into the solution when the liquid volume decreased to less than 50 mL. The solvent was evaporated from these mixtures by heating in an oven at 200 °C for 5 h. Finally, brown powders were obtained that changed to yellow after heating at 450 °C for 10 h. The obtained samples were named $Y_{0.9}Nd_{0.02}Tm_{0.03}Yb_{0.05}VO_4$-SG-CA and $Y_{0.9}Nd_{0.02}Tm_{0.05}Yb_{0.03}VO_4$-SG-CA, where the acronym CA refers to the chelating agent that was added to the reaction medium in its preparation, citric acid in these cases.

The same procedure was followed for the synthesis of the other two samples with the same compositions ($Y_{0.9}Nd_{0.02}Tm_{0.03}Yb_{0.05}VO_4$ and $Y_{0.9}Nd_{0.02}Tm_{0.05}Yb_{0.03}VO_4$) but withMA addition as a chelating agent instead of CA. In both cases, upon maleic acid addition, a color change from cloudy yellowish orange to transparent orange-brown was observed. The gel phases were then heated at 550 °C for 10 h. The obtained samples were named $Y_{0.9}Nd_{0.02}Tm_{0.03}Yb_{0.05}VO_4$-SG-MA and $Y_{0.9}Nd_{0.02}Tm_{0.05}Yb_{0.03}VO_4$-SG-MA, respectively, where the acronym

MA refers to the chelating agent added to the reaction medium.

2.2. Hydrothermal synthesis

Samples of the same compositions described above were also prepared by HT synthesis. Stoichiometric amounts of yttrium, erbium, neodymium and ytterbium nitrates were added into two beakers and dissolved in 40 mL of distilled water. The two resulting clear solutions were heated to 100 °C and stirred at 500 rpm on electric plates. After 15 min, solutions of 0.25 g of NH_4VO_3 dissolved in 20 mL of water were added to the nitrate solutions. All mixed solutions turned to an intense yellow color due to the vanadate ions presence. Fifteen minutes later, urea was added in a 1:1 M ratio regarding to the amount of NH_4VO_3 added and the pH of solutions was 4–5. After 15 min, CA was added, giving rise to blue solutions without any change in their pH.

After 15 min of reaction, NH_3 (32 %) was added until a pH of 9 is reached. The samples were then placed in an oven at 200 °C for 2 h to remove the solvent and burn the organic matter. The brown powders obtained were then redissolved in 30 mL of water and placed in autoclaves for heat treatment at 180 °C for 12 h. The resulting powders were washed with a 1:1 deionized water/ethanol mixture and centrifuged, drying at 50 °C.

The same procedure was followed for the synthesis of two samples with the same compositions described above, but using maleic acid as a chelating agent. Finally, the two powders obtained were heated at a higher temperature to increase their crystallinity (at 550 °C for 10 h for samples prepared with MA addition and at 450 °C for 10 h for those with CA). The obtained samples were called $Y_{0.9}Nd_{0.02}Tm_{0.03}Yb_{0.05}VO_4$-HT-MA, $Y_{0.9}Nd_{0.02}Tm_{0.05}Yb_{0.03}VO_4$-HT-MA, $Y_{0.9}Nd_{0.02}Tm_{0.03}Yb_{0.05}VO_4$-HT-CA and $Y_{0.9}Nd_{0.02}Tm_{0.05}Yb_{0.03}VO_4$-HT-CA, respectively.

2.3. Coating tests with TEOS

The Stöber method was used to carry out the coating tests [19]. 0.1 g of the corresponding orthovanadate samples were deposited in two-neck round-bottom flasks and dispersed in a mixture of 50 mL of water and 15 mL of ethanol. These dispersions were then subjected to an ultrasonic bath at 30 °C for 5 min. The presence of ethanol in the reaction medium facilitates the adhesion of the O-Si-O-Si-O polymer network to the surfaces of the particles present in the reaction medium [4,5,13]. Next, 10 mL of NH_3 (30 %) were added under continuous stirring and heating at 75 °C [4,5,20], acting as a catalyst for the coating process. After homogenizing the solutions, 1 mL of tetraethyl orthosilicate, $Si(OC_2H_5)_4$, TEOS (Merck) was added via syringe in amounts of 0.1 mL every 15 min. During this time, both heating and stirring were maintained. Finally, the mixtures were centrifuged to separate the precipitate, which was then washed with a 1:1 deionized water/ethanol solution and dried at 75 °C. The resulting white powders were called with the same name as the corresponding sample and adding @SiO_2.

2.4. Characterization techniques

X-ray diffraction (XRD) patterns of the synthesized samples were recorded on a PANalytical XPERT-PRO diffractometer with Cu $K_{\alpha 1}$ radiation in the 10–70° range in units of (2θ), using a step size of 0.04° and a step time of 1 s. The instrumental broadening of the diffraction peaks was calibrated by using the LaB6 standard NIST SRM 660b.

The average crystallite size of samples was calculated from XRD profiles using the Scherrer formula $= \frac{0.89\,\lambda}{\beta\,\cos\,\theta}$, where λ is the X-ray wavelength, β is the full width at half maximum (FWHM), and θ is the diffraction angle.

Fourier transform infrared spectroscopy (FTIR) spectra were registered employing a Spectrum Two FT-IR spectrophotometer and pressing the powder against a diamond. Measurements were taken in the 400-4000 cm^{-1} range with a resolution of 4 cm^{-1}.

Morphological characterization of the synthesized samples was carried out by transmission electron microscopy (TEM) using a JEOL JEM 2100F microscope operating at 200 kV, equipped with a field emission electron gun that provides a point resolution of 0.19 nm. To obtain the images, samples were dispersed in *n*-butanol and drops of the corresponding suspension were deposited on carbon-coated copper grids.

To study the UC and DS processes upon excitation at 808 and 980 nm, PL spectra of the samples were obtained. Powdered samples were deposited on glass microscope slides, sealed with coverslips, and placed in a home-made microscope equipped with a 10x objective (0.25 NA). Single-mode diode lasers were used for excitation. To evaluate the PL emission of the investigated samples in the UV-visible-NIR-II-III electromagnetic spectrum, both solid powder and dispersed samples (0.1 mg/mL in distilled water) were analyzed using two different laser wavelengths (808 and 980 nm).

The UC emission spectra were obtained by coupling the system to a Horiba i320 monochromator with a CCD camera (Horiba synapse). The spectra were recorded in the wavelength ranges of 350–750 nm and 350–850 nm with photoexcitation at 980 nm and 808 nm, respectively. These UC emission processes were also investigated in 0.1 mg/mL dispersions in distilled water, using both 980 and 808 nm diode lasers set at 62.6 mW and 53.9 mW, respectively.

For DS emission processes, the powder samples were investigated in the 970–1700 nm wavelength range at 808 nm excitation, using an Ocean Insigth NIRQuest spectrometer coupled to the system. Optical filters were incorporated before the detectors to block the laser radiation in all PL experiments.

3. Results and discussion

3.1. X-ray diffraction studies

Fig. 1 shows XRD patterns of samples synthesized by both the sol-gel and hydrothermal methods. All diffraction maxima can be indexed to a tetragonal symmetry of space group $I4_1/amd$ and Z = 4, compatible with the zircon-type structure of the YVO_4 oxide (reference JCPDS file 01-082-1968). No additional diffraction maxima are observed from other crystalline phases under the measurement conditions, confirming that the lanthanide ions were successfully incorporated into the lattice substituting Y^{3+} ions and revealing the purity of the samples. In addition, from the intensity values of the XRD profiles, a higher crystallinity of the powder samples prepared by sol-gel is observed.

Table 1 shows the cell parameters determined for all obtained samples from the XRD profiles of Fig. 1 using the ChekCell program. This program uses mathematical models to fit the experimental data to a hypothetical unit cell. Considering the positions of the diffraction maxima and using Bragg's law, the lattice parameters a, b, c and the unit cell angles (α, β, γ) are calculated.

The calculated cell parameters for all obtained samples are lower than those of YVO_4. This result can be justified by considering the ionic radii of Nd^{3+}, Tm^{3+} and Yb^{3+} ions that partially replace the Y^{3+} ions in their zircon-type structure [r Ln^{3+} (i.c. 8) → Y^{3+} = 1.019 Å, Nd^{3+} = 1.109 Å, Tm^{3+} = 0.994 Å and Yb^{3+} = 0.985 Å] [21]. The ionic radii of the Tm^{3+} and Yb^{3+} ions are smaller than those of Y^{3+} ions, but it is not the case for Nd^{3+} ions. Thus, considering a fixed and relatively low neodymium content present in the compositions of all obtained samples, the variation in the parameters is as expected. Both parameters and cell volume are reduced with increasing thulium and ytterbium content.

Fig. 2 shows two different orientations of the zircon-type structure present in all investigated samples. This structure is composed of Y(Nd/Tm/Yb)O_8 bisdisphenoids that share edges generating zig-zag chains in the ac plane. Along the c axis, these bisdisphenoid chains are linked to [VO_4^{3-}] tetrahedra, sharing opposite edges between two parallel chain bidisphenoids [4,5,13].

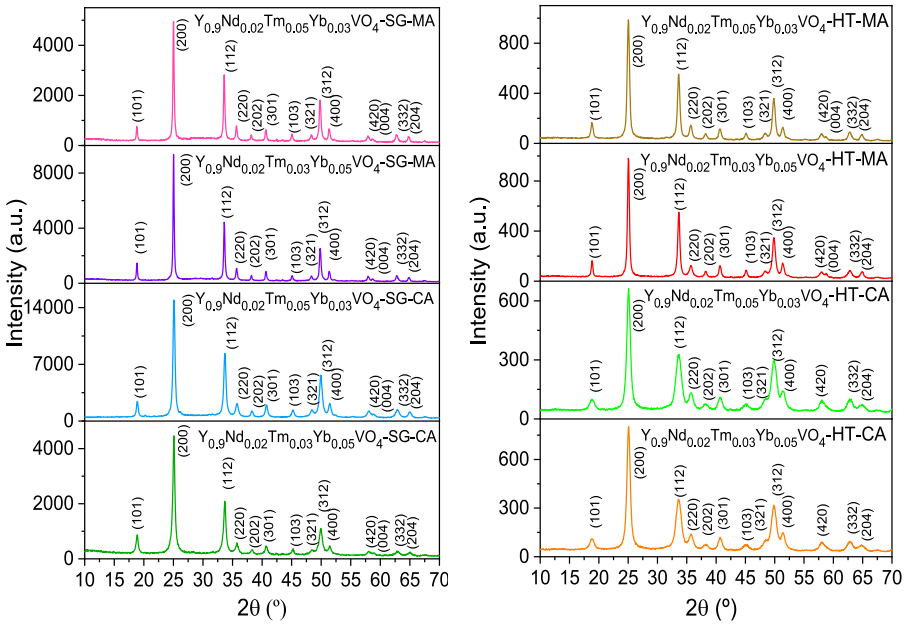

Fig. 1. XRD patterns of all synthesized samples.

Table 1
Crystallographic parameters of all investigated samples.

Sample	Calculated parameters		
	a = b (Å)	c (Å)	V (Å^3)
YVO_4 [JCPDS file card nº [01-082-1968] (data for comparison purposes)	7.1183	6.2893	318.68
Samples prepared by sol gel			
$Y_{0.9}Nd_{0.02}Tm_{0.03}Yb_{0.05}VO_4$-SG-CA	7.101 (4)	6.2623 (4)	315.83
$Y_{0.9}Nd_{0.02}Tm_{0.05}Yb_{0.03}VO_4$- SG-CA	7.097 (4)	6.2694 (5)	315.81
$Y_{0.9}Nd_{0.02}Tm_{0.03}Yb_{0.05}VO_4$- SG-MA	7.110 (3)	6.2830 (3)	317.67
$Y_{0.9}Nd_{0.02}Tm_{0.05}Yb_{0.03}VO_4$- SG-MA	7.114 (3)	6.2866 (3)	318.18
Samples prepared by hydrothermal synthesis			
$Y_{0.9}Nd_{0.02}Tm_{0.03}Yb_{0.05}VO_4$-HT-CA	7.106 (6)	6.275 (1)	316.91
$Y_{0.9}Nd_{0.02}Tm_{0.05}Yb_{0.03}VO_4$- HT-CA	7.105 (9)	6.287 (1)	317.35
$Y_{0.9}Nd_{0.02}Tm_{0.03}Yb_{0.05}VO_4$- HT-MA	7.106 (4)	6.2755 (4)	316.95
$Y_{0.9}Nd_{0.02}Tm_{0.05}Yb_{0.03}VO_4$- HT-MA	7.105 (2)	6.2825 (3)	317.16

3.2. FTIR characterization studies

Fig. 3 shows the FTIR spectra of all synthesized samples before and after being treated with TEOS (in darker color in each figure).

FTIR spectra of untreated samples exhibit two absorption bands at ca. 778 cm^{-1} and 453 cm^{-1}. These bands can be assigned to the asymmetric stretch vibration of the V-O bonds in the [VO_4^{3-}] units and to the asymmetric stretch vibration of the Y/Ln^{3+}-O bonds in the [Y(Nd/Tm/Yb)O_8] bisdisphenoids, respectively [5,17,22].

FTIR spectra of TEOS-treated samples show a broad band at 1080 cm^{-1} with a pronounced shoulder located at 1200 cm^{-1}, which is assignable to the asymmetric stretch vibration of the Si-O-Si bonds. This result indicates that TEOS has successfully reacted, and silica-coated samples were obtained [15]. In addition, the band located at ~ 453 cm^{-1} is now more intense than that in the FTIR spectra of non-TEOS-treated samples. This increase in intensity is due to the overlap of the Y/Ln^{3+}-O bond strain vibration band with the in-plane bending vibration of the Si-O bond [15,23,24]. Finally, a band at 950 cm^{-1} assignable to the stretching of Si-OH bonds of silanol groups present in the silica shell can also be observed. This very strong band completely overlaps with the asymmetric stretching vibration band of V-O bonds present in the [VO_4^{3-}] units, even strongly reducing its intensity, and therefore, it cannot be analyzed independently.

3.3. Transmission electron microscopy studies

TEM images of all investigated samples are shown in Figs. 4 and 5. The average particle size of these powders was determined using ImageJ software. In TEM images of samples prepared by sol-gel with MA addition (see Fig. 4), larger and less agglomerated particles with a spherical shape and size varying between 21 and 76 nm are observed. However, in TEM images of sol-gel synthesized samples with CA addition, highly agglomerated particles with spherical and oval shapes can be observed. Their size varies in the range between 11 and 34 nm, in good agreement with our previous works [4,5]. Obtained results show that the addition of a different chelating agent decisively influences the particle size, its morphology and its degree of agglomeration. In the samples prepared by sol-gel, it has been found that the MA addition originates particles with a larger spherical shape and less agglomerated, while the CA addition in the reaction medium generates samples of spherical and oval particles, of smaller size and highly agglomerated.

TEM images of the same samples prepared by hydrothermal synthesis (Fig. 5) show a similar rounded morphology but of smaller size than those prepared by the SG method, with a size between 15 and 37 nm for MA and 8–13 nm for CA. This result shows that these preparations favor obtaining samples with smaller particle sizes and it is evident that samples prepared with MA addition appear to present considerably less aggregation.

Because the same chelating agents were added to the reaction medium to carry out the synthesis of these samples, the differences in particle size must be attributed to the synthesis method used in each case. The HT method involves carrying out the synthesis at high

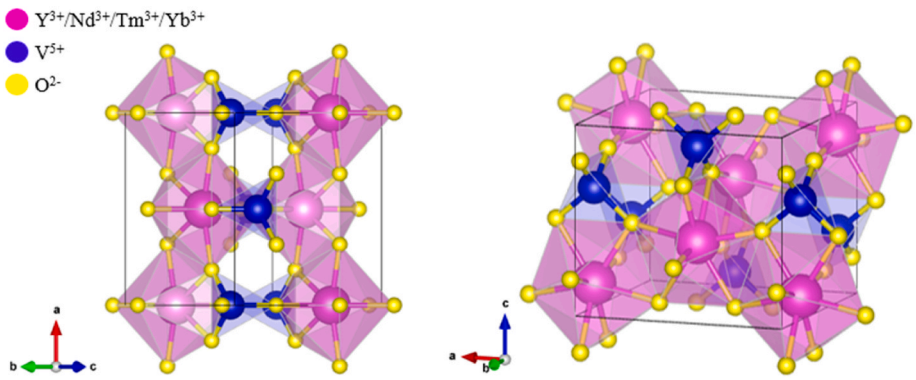

Fig. 2. Two perspectives of the zircon-type structure of the investigated samples generated with the VESTA program.

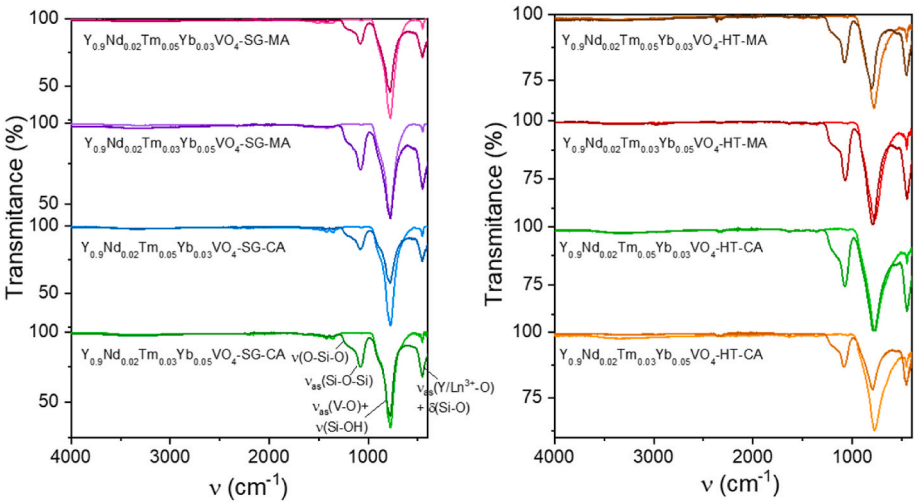

Fig. 3. Infrared (FTIR) spectra of all samples prepared by SG method and HT synthesis. FTIR of coated samples are shown in darker colour. (For interpretation of the references to color in this figure legend, the reader is referred to the Web version of this article.)

temperatures and pressures, which accelerates nucleation and promotes the formation and growth of smaller particles in a more controlled manner. On the other hand, the SG method uses milder temperature conditions during the gel formation and aging process, which leads to slower particle growth and causes particle aggregation, favouring the growth of these aggregates to give rise to larger particles.

It should be noted that the addition of MA and CA in the preparations carried out via hydrothermal means leads to samples of smaller particle size than those obtained and described in our previous works [4,5,13] and with a more homogeneous particle morphology.

TEM images of all TEOS-treated samples show encapsulated particles surrounded by a silica shell whose thickness varies from 4 to 13 nm, indicating that the coating process was successful. The progressive addition of small volumes of organosilane over the coating formation has influenced the formation of a thin and more homogeneous silica shell compared to that obtained by adding the same amount of TEOS at once, as described in previous works [4,22].

3.4. Photoluminescence (PL) studies

3.4.1. PL study of powder samples in the NIR II-III region under photoexcitation at 808 nm

For a comparative study, two samples with the same composition and chelating agent (MA) synthesized by the two different methods (SG and HT) were selected. Specifically, $Y_{0.9}Nd_{0.02}Tm_{0.05}Yb_{0.03}VO_4$-HT-MA and $Y_{0.9}Nd_{0.02}Tm_{0.05}Yb_{0.03}VO_4$-SG-MA samples. PL spectra of these powder samples registered under excitation at 808 nm and different pumping powers are shown in Fig. 6. Similar measurements performed for the remaining samples untreated with TEOS are included in Fig. S1 of the Supporting Information document.

Four DS emission bands are observed. These emission bands result from the absorption of laser energy by the Nd^{3+} ions and the subsequent effective energy transfer to Yb^{3+}. These electronic transits between levels give rise to maxima and minima of emission intensity, being the maximum emission intensity observed at 913 nm (Nd^{3+}: $^4F_{3/2} \rightarrow {}^4I_{9/2}$), 980 nm ($Yb^{3+}$: $^2F_{5/2} \rightarrow {}^4I_{9/2}$), 1062 nm ($Nd^{3+}$: $^4F_{3/2} \rightarrow {}^4I_{11/2}$) and the minimum at 1334 nm (Nd^{3+}: $^4F_{3/2} \rightarrow {}^4I_{13/2}$) [1,16,25]. In the NIR II-III region, Tm^{3+} ion emission bands were not observed. This fact can be justified by considering the ground state absorption (GSA) that occurs in the ground state $^3H_4$ of the Tm^{3+} ions and producing an excitation towards the $^3H_6$ state by absorption and re-emission of a photon at the same wavelength ($^3H_4 \rightarrow {}^3H_6$). This process takes place without energy losses, as these are non-radiative transitions, (see Fig. 7), which shows the energy levels diagram of Nd^{3+}, Yb^{3+} and Tm^{3+} ions. Consequently, the lowest energy states are not populated that would typically lead to NIR II-III emission.

Considering PL spectra of Fig. 6 and S1, it should be noted that the intensity ratio between the most intense band of Nd^{3+} and Yb^{3+} ions provide information about the excited state absorption (ESA) and energy transfer (ET) processes taking place between these two ions. As can be seen in Fig. 8, in the spectrum of samples with the lowest thulium content (0.03), the intensity ratio value between the most intense Nd^{3+} and Yb^{3+} bands is always higher compared to that of the samples containing 0.05. This result can be explained by considering that the $^3H_4$

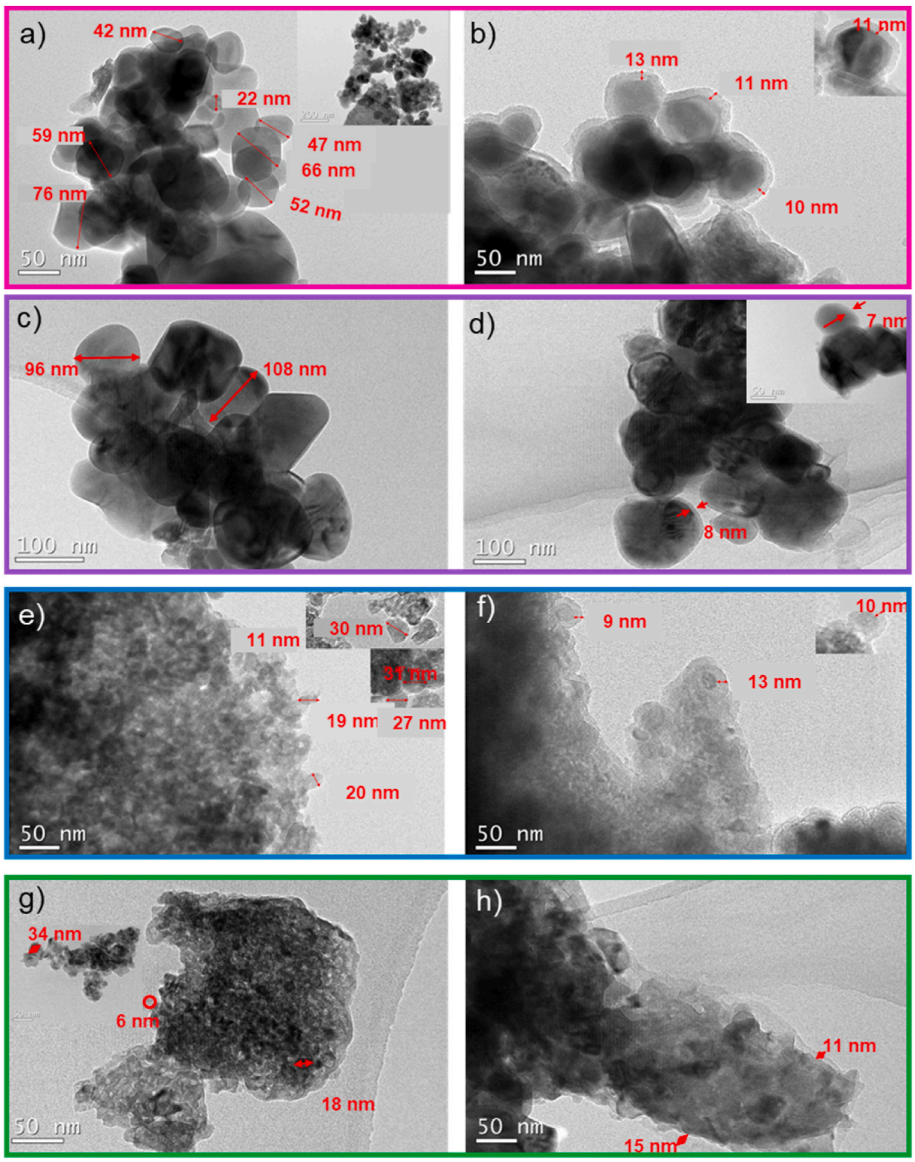

Fig. 4. *TEM images of the uncoated and silica-coated samples synthesized by the SG method: a) $Y_{0.9}Nd_{0.02}Tm_{0.05}Yb_{0.03}VO_4$-SG-MA, b) $Y_{0.9}Nd_{0.02}Tm_{0.05}Yb_{0.03}VO_4$-SG-MA@$SiO_2$, c) $Y_{0.9}Nd_{0.02}Tm_{0.03}Yb_{0.05}VO_4$-SG-MA, (d) $Y_{0.9}Nd_{0.02}Tm_{0.03}Yb_{0.05}VO_4$-SG-MA@$SiO_2$, e) $Y_{0.9}Nd_{0.02}Tm_{0.05}Yb_{0.03}VO_4$-SG-CA (f) $Y_{0.9}Nd_{0.02}Tm_{0.05}Yb_{0.03}VO_4$-SG-CA@$SiO_2$, (g) $Y_{0.9}Nd_{0.02}Tm_{0.03}Yb_{0.05}VO_4$-SG-CA and (h) $Y_{0.9}Nd_{0.02}Tm_{0.03}Yb_{0.05}VO_4$-SG-CA@$SiO_2$.* (For interpretation of the references to color in this figure legend, the reader is referred to the Web version of this article.)

level of Tm^{3+} ions is also excited under 808 nm radiation. Thus, by reducing the thulium content present in the sample, the radiation absorbed by the Nd^{3+} ions increases, making the ET of the Yb^{3+} ions much more efficient.

Fig. 8 also shows that the intensity ratio is ≤ 1 in the samples prepared by SG and the HT methods and with the CA addition, while this value is greater than 1 in those prepared with MA, indicating that in the spectra of the latter the bands of the Nd^{3+} ions are slightly more intense than those of the Yb^{3+} ions. These results highlight the significant role and influence that the lanthanide ion content and the synthesis conditions exert on the intensity of luminescent emission in this type of samples.

The study of the dependence of the PL emission intensity on the pump laser power provides information regarding the underlying emission processes in the investigated samples.

The power dependence of luminescence provides insights into the underlying emission processes. Fitting the data to a linear Ln-Ln model enables the determination of the number of absorbed laser photons required to generate emission at a specific wavelength. In this case, it corresponds to a DS process, where a single high-energy photon from the laser source is involved in the emission of photons by the material. This approach also facilitates the characterization of emission efficiency at different excitation power levels, suggesting that the material efficiently converts the absorbed energy into light when linearity is maintained at high excitation powers.

In Figs. 6 and S1, the PL spectra show what happens in a DS process, where a single high-energy photon from the laser source is involved in the emission of the two measured samples. The intensity of the PL emission depends on the laser power, and this allows to determine the number of photons that are involved in DS processes, which can be determined by the relationship between the PL intensity (I_{PL}) and the pumping laser power (I_P) by the following expression:

$$I_{PL}\alpha\ (I_P)^n \quad (1)$$

where α is a proportionality factor and n the number of photons [26,27]. The graphs inserted in Fig. 6 and S1 show the variation in band

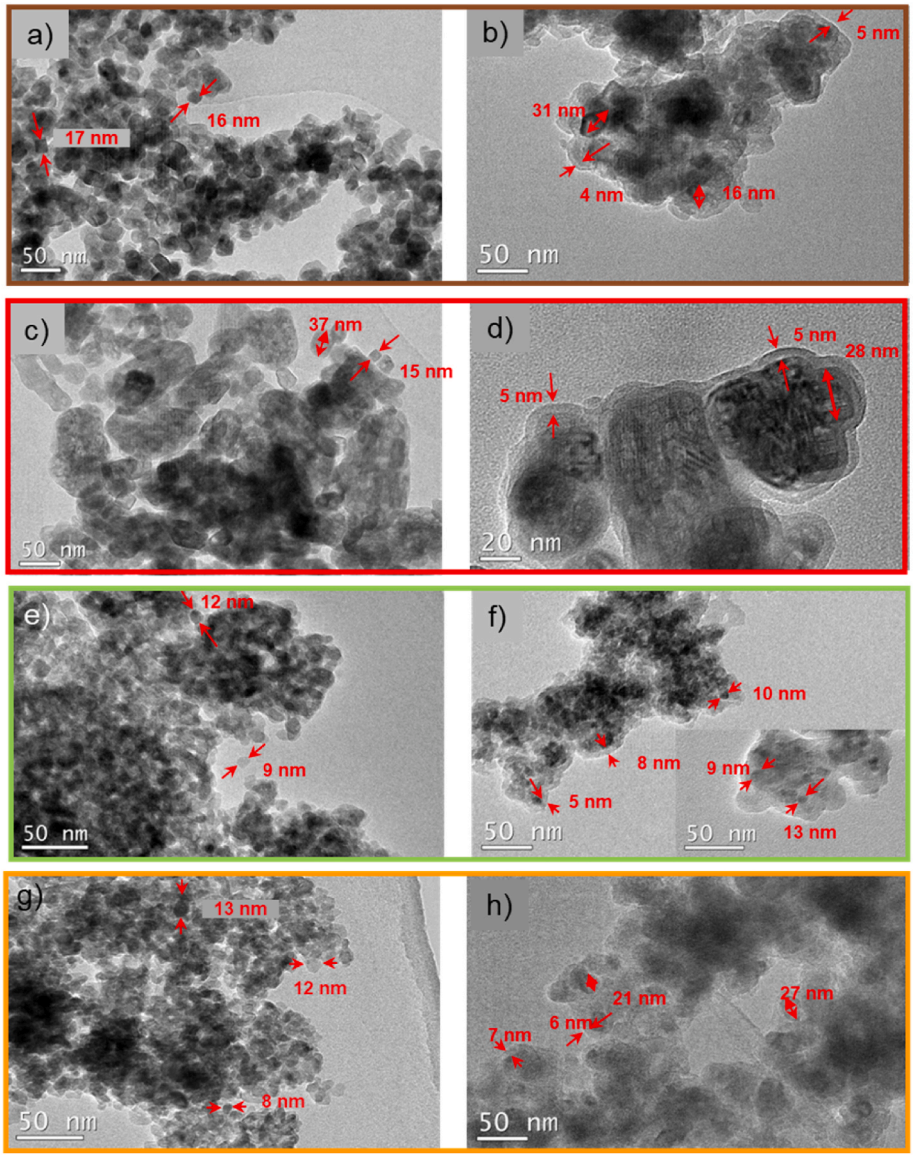

Fig. 5. TEM images of the uncoated and silica-coated samples synthesized by HT synthesis: (a) $Y_{0.9}Nd_{0.02}Tm_{0.05}Yb_{0.03}VO_4$-HT-MA, (b) $Y_{0.9}Nd_{0.02}Tm_{0.05}Yb_{0.03}VO_4$-HT-MA@$SiO_2$, (c) $Y_{0.9}Nd_{0.02}Tm_{0.03}Yb_{0.05}VO_4$-HT-MA, (d) $Y_{0.9}Nd_{0.02}Tm_{0.03}Yb_{0.05}VO_4$-HT-MA@$SiO_2$, (e) $Y_{0.9}Nd_{0.02}Tm_{0.05}Yb_{0.03}VO_4$-HT-CA, (f) $Y_{0.9}Nd_{0.02}Tm_{0.05}Yb_{0.03}VO_4$-HT-CA@$SiO_2$, (g) $Y_{0.9}Nd_{0.02}Tm_{0.03}Yb_{0.05}VO_4$-HT-CA and (h) $Y_{0.9}Nd_{0.02}Tm_{0.03}Yb_{0.05}VO_4$-HT-CA@$SiO_2$.

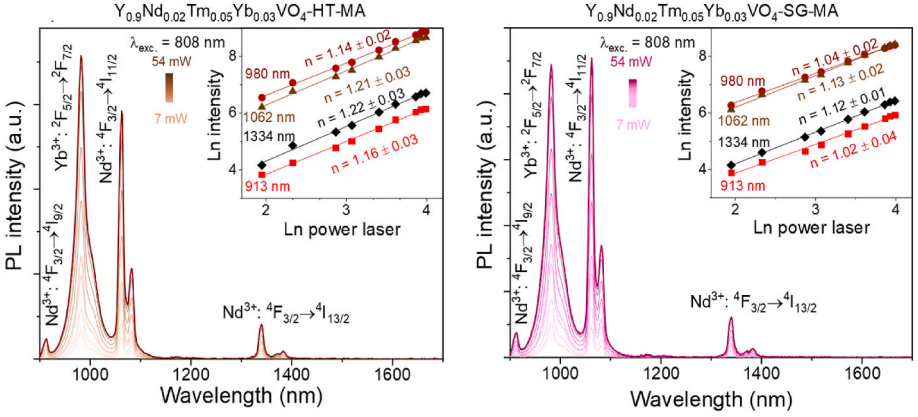

Fig. 6. *PL spectra of powder samples in the* NIR region. *Inset graphs show the logarithm of the peaks intensity as a function of logarithm of the applied laser power (dots) along with their linear fits (lines).*

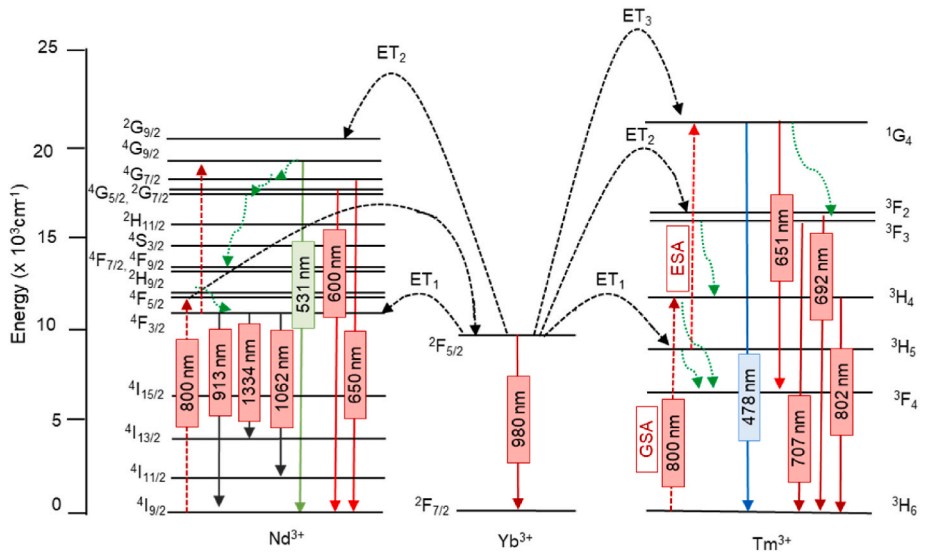

Fig. 7. Schematic energy levels diagram of Nd^{3+}, Yb^{3+} and Tm^{3+} ions, also showing PL mechanisms occurring after photoexcitation at 808 nm and possible ET processes occurring between the levels of Nd^{3+} and Yb^{3+} ions towards those of the Tm^{3+} ion.

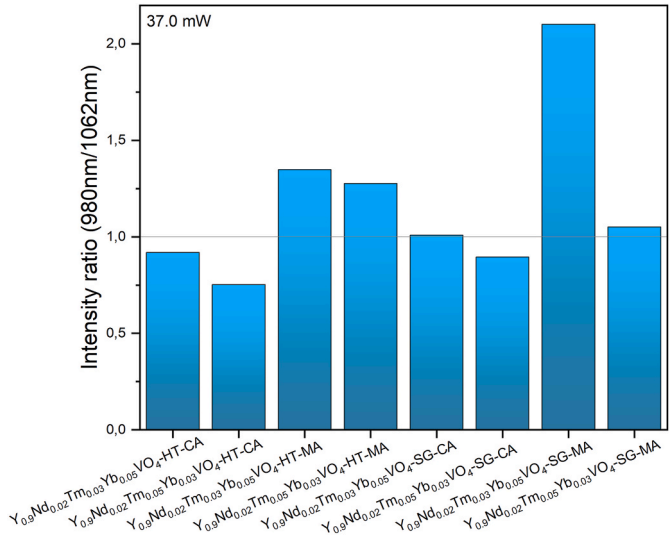

Fig. 8. Intensity ratio of the 980 nm/1062 nm bands at 37.0 mW.

intensities with applied power. All these linear fits show that a single photon is involved in this type of mechanism due to the Stokes process taking place by emitting radiation of lower energy than that of the photoexcitation source [1].

3.4.2. *UC study of powder samples under photoexcitation at 808 and 980 nm*

Considering that the intensity ratio value between the most intense band of Nd^{3+} and Yb^{3+} ions is higher for samples prepared by both SG and HT synthesis with MA addition, this study was only carried out on the $Y_{0.9}Nd_{0.02}Tm_{0.05}Yb_{0.03}VO_4$-SG-MA and $Y_{0.9}Nd_{0.02}Tm_{0.05}Yb_{0.03}VO_4$-HT-MA powder samples.

Fig. 9 shows the UC spectra recorded under photoexcitation at 808 and 980 nm and at different laser powers. Similar UC spectra performed for the remaining samples are included in Figs. S2–S4 of the Supporting Information. Most of the observed emission bands in these spectra can be attributed to the population of 4f energy levels of Tm^{3+} ions, which occur due to the ET process by the sensitizer ions.

When these samples are excited at 808 nm, according to the proposed mechanism (see Fig. 7), Nd^{3+} ions end up populating their $^4F_{5/2}$ excited state. Then, another non-radiative relaxation takes place to the $^4F_{3/2}$ level. Subsequently, energy from this energy level is transferred by ET resonance to the $^2F_{5/2}$ excited level of Yb^{3+} ions. In this situation, although the 808 nm laser radiation has enough energy to populate the $^4F_{5/2}$ level of Nd^{3+} ions, it is insufficient to excite electrons directly to the excited state of Yb^{3+} ions. For this reason, Nd^{3+} ions initially act as sensitizers by transferring energy to the $^2F_{5/2}$ excited level of Yb^{3+} ions and these act as bridge ions, transferring energy to the $^1G_4$, $^3F_{2,3}$ and $^3H_5$ excited states of Tm^{3+} ions [1,6,7,28–30].

Table 2 shows the slopes values (n) obtained from the linear fits of the variation of the band intensities observed in the UC spectra plotted in Figs. 9 and S2 with the laser power applied under excitation at 808 nm. No significant differences were found related to the sample preparation method or the shape and size of the particle that makes up each sample. In all cases, the obtained values confirm a typical two-photon UC process that follows the sequence $Nd^{3+}\rightarrow Yb^{3+}\rightarrow Tm^{3+}$ and takes place when an anti-Stokes phenomenon occurs. Along this sequence, the excited states of Tm^{3+} ions are initially populated, giving rise to radiative transitions at values of 478 nm ($^1G_4\rightarrow{}^3H_6$), 650 nm ($^1G_4\rightarrow{}^3F_4$), 692 nm ($^3F_2\rightarrow{}^3H_6$) and 707 nm ($^3F_3\rightarrow{}^3H_6$) [46, 63–64, 73].

Additionally, since Tm^{3+} ions have energy levels with energy gaps close to 808 nm, direct excitation to the $^3H_4$ state through GSA and subsequent multiphonon relaxation to the $^3H_5$ excited state becomes possible. This state can then absorb a second photon via ESA, populating the $^1G_4$ state. Non-radiative transitions from $^1G_4$ to the $^3F_{2,3}$ levels can also give rise to emissions at 692 and 707 nm [3,7,27,31,32].

Fig. 10 shows the ET processes that occur upon irradiation of the synthesized samples at 980 nm. The UC process shown in the spectra of Figs. 9 and S3 takes place by the absorption of 980 nm laser radiation by Yb^{3+} ions, exciting electrons from the ground state to the $^1G_4$, $^3F_{2,3}$ and $^3H_5$ excited levels with the consequent $^2F_{5/2}\rightarrow{}^2F_{7/2}$ radiative transition. The Yb^{3+} ions then transfer energy to three different excited levels of Tm^{3+} ions through phonon-assisted ET, which is required to bridge the energy gap between the excited states of thulium and ytterbium ions. These ET processes are accompanied by non-radiative transitions ($^3H_5\rightarrow{}^3F_4$ and $^3F_{2,3}\rightarrow{}^3H_4$) that occur with subsequent phonon emission. On the other hand, Tm^{3+} ions can also directly absorb radiation through GSA process, leading to the population of the $^3H_5$ excited state, followed by the population of the $^1G_4$ and $^3F_{2,3}$ states through ESA [27,29,31]. The same bands can also be observed under 808 nm excitation (Fig. 11): 478 nm ($^1G_4\rightarrow{}^3H_6$), 530 nm $^4G_{9/2}\rightarrow{}^4I_{9/2}$, 600 nm $^4G_{7/2,\ 5/2}\rightarrow{}^4I_{9/2}$, 650

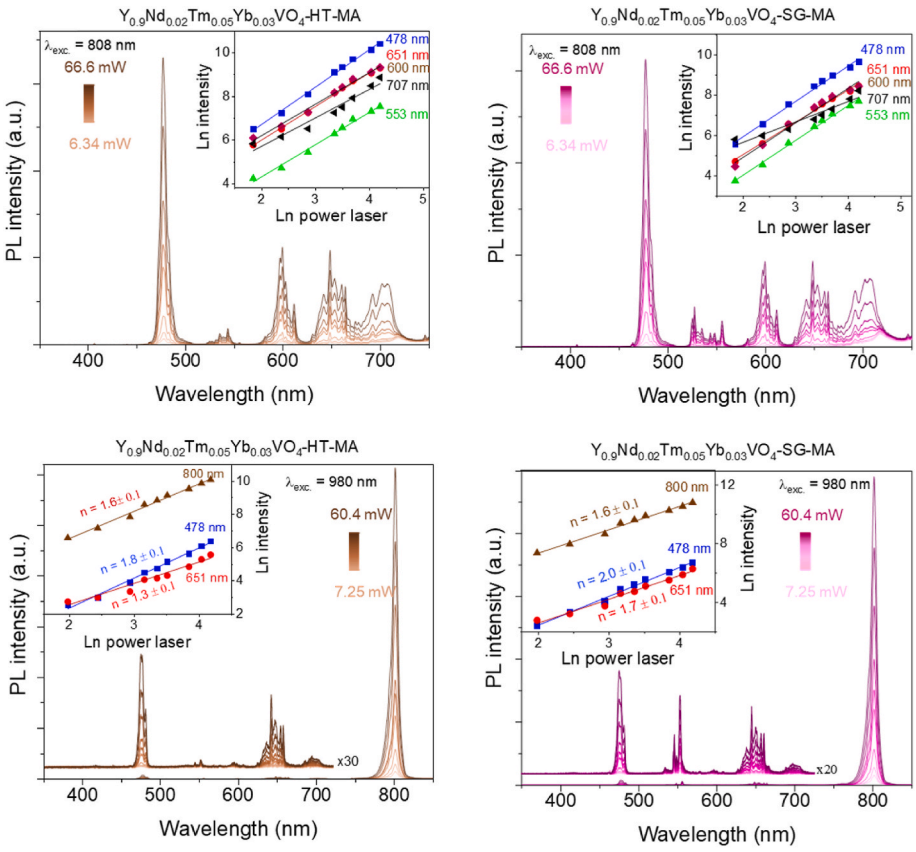

Fig. 9. *UC spectra of samples prepared by sol-gel and synthesis hydrothermal with MA addition* under photoexcitation at 808 and 980 nm. *Inset graphs show the* Ln*(I)-Ln(P) variations with their linear fits (lines).*

Table 2
Slope value of Ln-Ln variations obtained by exciting at 808 nm.

Sample	Slope value (n)				
	478 nm	550 nm	600 nm	651 nm	707 nm
Samples prepared by sol gel					
$Y_{0.9}Nd_{0.02}Tm_{0.03}Yb_{0.05}VO_4$-SG-CA	1.7 ± 0.1	1.5 ± 0.1	1.5 ± 0.1	1.6 ± 0.1	1.3 ± 0.1
$Y_{0.9}Nd_{0.02}Tm_{0.05}Yb_{0.03}VO_4$-SG-CA	1.67 ± 0.02	1.14 ± 0.02	1.35 ± 0.04	1.48 ± 0.02	1.1 ± 0.1
$Y_{0.9}Nd_{0.02}Tm_{0.03}Yb_{0.05}VO_4$-SG-MA	1.6 ± 0.1	1.4 ± 0.1	1.5 ± 0.1	1.5 ± 0.1	1.9 ± 0.1
$Y_{0.9}Nd_{0.02}Tm_{0.05}Yb_{0.03}VO_4$-SG-MA	1.8 ± 0.1	1.7 ± 0.1	1.7 ± 0.1	1.6 ± 0.1	1.0 ± 0.1
Sample prepared by hydrothermal synthesis					
$Y_{0.9}Nd_{0.02}Tm_{0.03}Yb_{0.05}VO_4$-HT-CA	1.74 ± 0.02	1.3 ± 0.1	1.45 ± 0.03	1.60 ± 0.02	1.3 ± 0.2
$Y_{0.9}Nd_{0.02}Tm_{0.05}Yb_{0.03}VO_4$-HT-CA	1.71 ± 0.04	1.5 ± 0.1	1.4 ± 0.1	1.54 ± 0.04	1.3 ± 0.1
$Y_{0.9}Nd_{0.02}Tm_{0.03}Yb_{0.05}VO_4$-HT-MA	1.67 ± 0.03	1.4 ± 0.1	1.5 ± 0.1	1.52 ± 0.03	0.9 ± 0.1
$Y_{0.9}Nd_{0.02}Tm_{0.05}Yb_{0.03}VO_4$-HT-MA	1.71 ± 0.04	1.5 ± 0.1	1.4 ± 0.1	1.54 ± 0.04	1.3 ± 0.1

nm ($^1G_4 \rightarrow {}^3F_4$), 692 nm ($^3F_2 \rightarrow {}^3H_6$) and 707 nm ($^3F_3 \rightarrow {}^3H_6$), and the most intense emission band at 802 nm is the contribution of Tm^{3+} ($^3H_4 \rightarrow {}^3H_6$) and Nd^{3+} ($^4F_{7/3,\ 9/3} \rightarrow {}^4I_{9/2}$) [3,29–31].

Regarding the emission bands at 530 and 600 nm observed in UC spectra of Fig. 9, S2 and S3, it should be noted that they are not characteristic of thulium ions. Therefore, we propose that Yb^{3+} ions transfer energy back to Nd^{3+} ions, allowing the high-energy $^2G_{9/2}$ level to be populated and, from non-radiative transitions, the following sequence would take place: $^4G_{9/2} \rightarrow {}^4I_{9/2}$ and $^4G_{7/2,\ 5/2} \rightarrow {}^4I_{9/2}$, which would explain the presence in these spectra of bands centered at 530 and 600 nm with green and red emission, respectively [30].

UC spectra of samples prepared by SG and HT synthesis showing the emission bands corresponding to $^3F_{2,3} \rightarrow {}^3H_6$ electronic transits at different laser pumping powers are shown in Fig. 11 and S4 of the Supporting Information.

In all cases, the emission band with maximum at 707 nm is broad due to the overlapping of the emission bands at 692 and 702 nm from close energy excited states. The proximity in energy favours multiphonon relaxations from $^3F_2$–$^3F_3$, so the population of both levels is guaranteed. In all UC spectra, the intensity of these emission bands increases with laser power in a similar proportion. However, the emission intensity at 718 nm increases up to around 21.5 mW and then remains constant. This can be explained due to the fast multiphonon relaxations occurring from the $^3F_2$ level to the $^3F_3$ level, and to the proximity in energy between levels. As the energy gap from the $^3F_3$ level to the lower $^3H_4$ state is much larger (2100 cm^{-1}), the non-radiative decays to the $^3H_4$ state are very slow, causing the population to increase in the $^3F_3$ level and leading to a more intense emission [32]. Fig. 11d also shows the two-slope dependence of the PL intensity with the laser power, indicating that a single-pseudo-photon emission process has taken place because of the ET process between Tm^{3+} ions [27]. Furthermore, the $^3F_3 \rightarrow {}^3H_6$ emission band is more intense at lower laser powers and this result can be justified by the decrease of non-radiative transits due to the heating of the sample by the laser power.

3.4.3. UC study of some samples investigated in dispersion under photoexcitation at 808 and 980 nm

To determine the potential application of some investigated samples in biological media and the influence of the aqueous medium on the luminescent emission capacity of these samples, a preliminary UC study

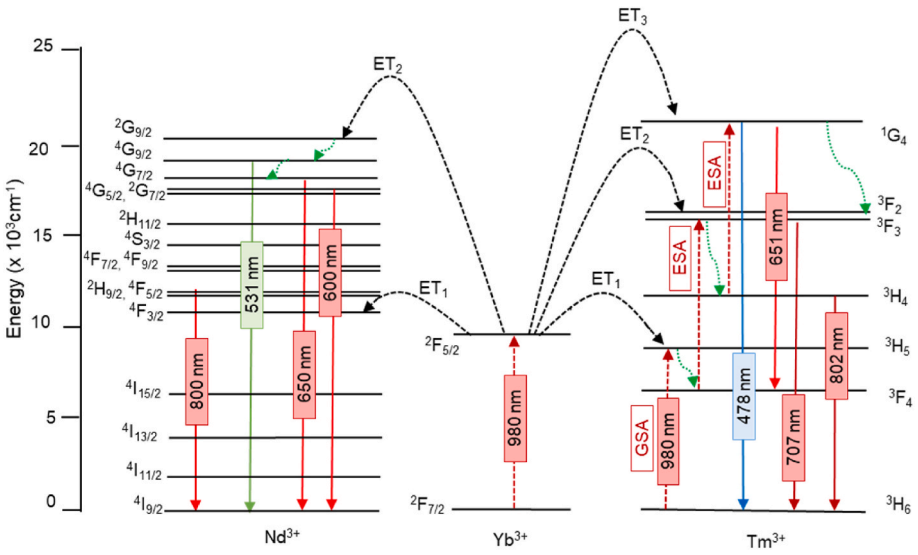

Fig. 10. Diagram of the ET process occurred between Nd^{3+} and Yb^{3+} ions to the Tm^{3+} ions when excited with 980 nm laser energy.

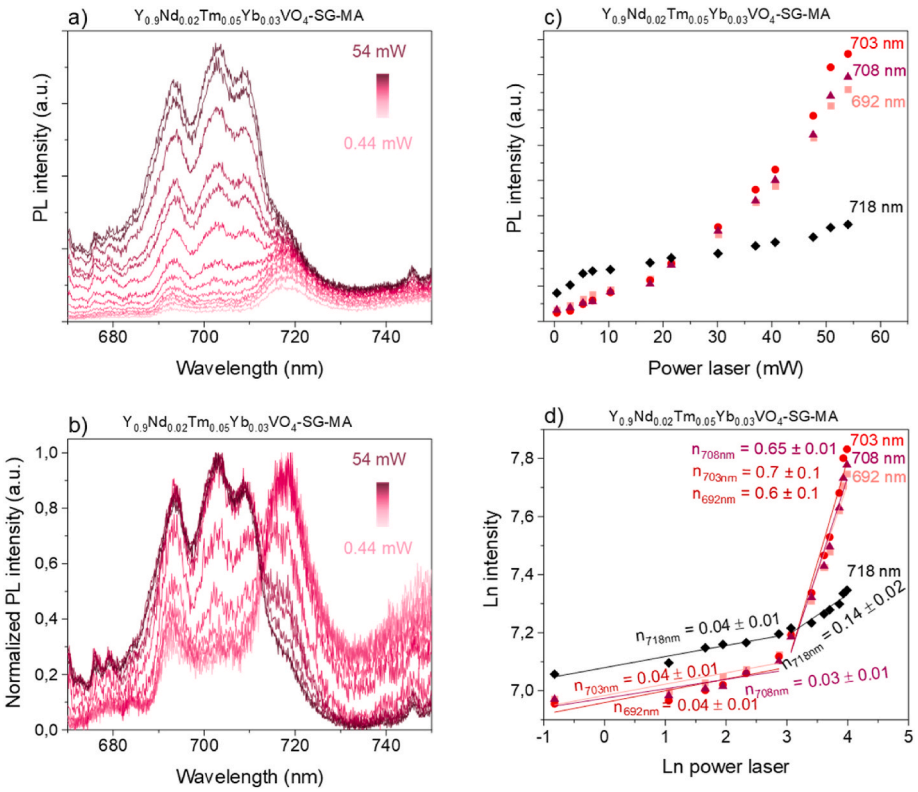

Fig. 11. (a) UC spectra of samples prepared by sol-gel showing $^3F_{2,3} \rightarrow {}^3H_6$ emission bands at different laser pumping powers, (b) normalized PL intensity of the $^3F_{2,3} \rightarrow {}^3H_6$ emission bands, (c) PL intensity vs. pumping power, (d) Ln(I)-Ln(P) variations.

of uncoated and silica-coated samples with different thulium content was performed.

Fig. 12 shows the UC spectra of coated and silica-coated $Y_{0.9}Nd_{0.02}Tm_{0.03}Yb_{0.05}VO_4$ and $Y_{0.9}Nd_{0.02}Tm_{0.05}Yb_{0.03}VO_4$ water-dispersed samples (0.1 mg/mL) obtained after photoexcitation with an 808 nm laser.

Samples with lower concentration of activator ion (Tm^{3+}) shows a higher emission intensity. By contrast, in the spectra of the silica-coated samples a reduction in the emission intensity in the band at 480 nm is observed, while the intensity of the bands at 600 and 650 nm remains constant and even increases. These results can be justified by considering that the samples with a smaller particle size have a larger surface area per unit volume and this causes, them to be surrounded by a greater number of -OH groups in aqueous dispersion. The high-energy vibrational frequencies (3200-3500 cm^{-1}) of these groups induce non-radiative relaxations. For this reason, low emission intensity is observed in $Y_{0.9}Nd_{0.02}Tm_{0.03}Yb_{0.05}VO_4$-SG-CA and $Y_{0.9}Nd_{0.02}Tm_{0.05}Yb_{0.03}VO_4$-SG-CA samples with smaller particle size [22,33,34], as has been evident in the TEM images. Furthermore, the high aggregation of the particles in aqueous dispersion reduces the

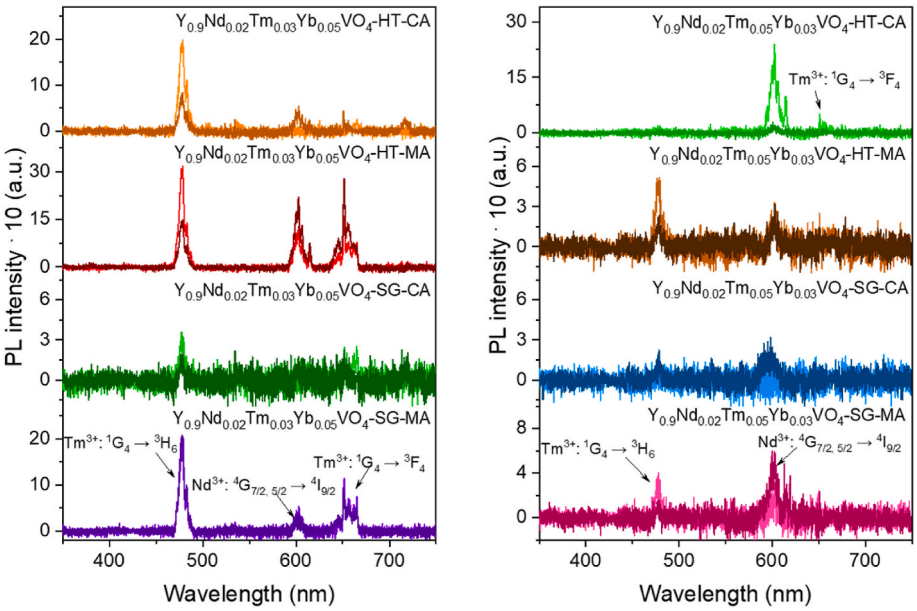

Fig. 12. UC emission spectra recorded after irradiation at 808 nm of coated and silica-coated $Y_{0.9}Nd_{0.02}Tm_{0.03}Yb_{0.05}VO_4$ and $Y_{0.9}Nd_{0.02}Tm_{0.05}Yb_{0.03}VO_4$ water-dispersed samples.

emission properties of the mentioned samples [26]. On the other hand, the silica coating causes the presence of Si-OH groups on the surface, which act as fluorescence intensity quenchers, as we have already described in previous investigations [4,13,26,34].

Fig. 13 shows the UC spectra of the 0.1 mg/mL water-dispersed samples excited by a 980 nm laser. Consistent with the results obtained after excitation at 808 nm, the samples exhibiting the lowest concentrations of Tm^{3+} demonstrate the highest emission intensities. An exception to this trend is noted in the $Y_{0.9}Nd_{0.02}Tm_{0.05}Yb_{0.03}VO_4$-HT-MA sample, which displays the most intense emission band at 802 nm. Existing literature indicates that samples characterized by low percentages of activator ions tend to exhibit the highest UC emission intensity [2,30]. Samples with lower percentage of Tm^{3+} exhibit intense emission in the 480 and 660 nm bands relative to the 802 nm band, indicating that a lower amount of Yb^{3+} ions enhances the UC energy transfers to the Tm^{3+} ions. However, for lasers under 980 nm, the presence of silica considerably reduces the emission intensity, as observed with excitation at 808 nm.

The emission study of the investigated samples shows that after excitation at both 808 and 980 nm, $Y_{0.9}Nd_{0.02}Tm_{0.03}Yb_{0.05}VO_4$-HT-MA sample exhibits the best luminescent emission intensity in the UV–visible–NIR I range of the electromagnetic spectrum. In addition, this sample can emit efficiently and with total transparency in the biological window between 800 and 1700 nm, making it the most suitable sample as a luminescent probe in bioimaging [30].

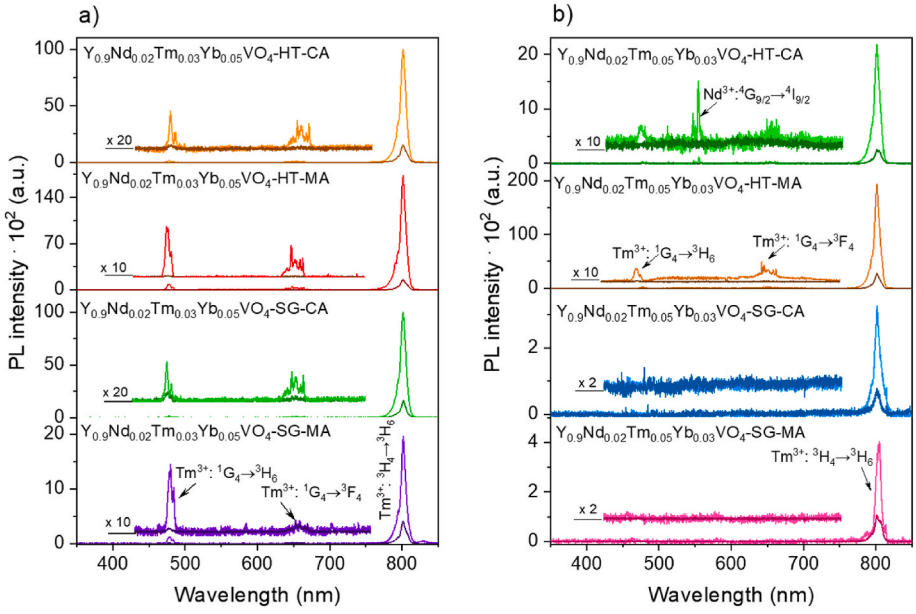

Fig. 13. UC emission spectra after irradiation at 980 nm of coated and uncoated 0.1 mg/mL (a) $Y_{0.9}Nd_{0.02}Tm_{0.03}Yb_{0.05}VO_4$ and (b) $Y_{0.9}Nd_{0.02}Tm_{0.05}Yb_{0.03}VO_4$ water-dispersed samples.

4. Conclusions

Crystalline samples have been successfully prepared by SG and HT methods with MA and CA addition. The use of complexing agents has been shown to inhibit the particle growth process, allowing the preparation of samples with rounded particles of nanometric size by both methods. In addition, the selection of the synthesis method in combination with the chelating agent has been shown to influence the particle agglomeration degree. Large agglomerations were observed in the sample prepared by the SG method with CA addition, as seen in the TEM images. The silica presence was confirmed by FTIR spectra, and the thickness of the silica coating shell was determined from TEM images to be 5–13 nm, where larger particles were also observed in samples prepared by SG. The extensive PL study has allowed us to analyze the fluorescent emission of samples investigated in both powder and aqueous dispersion after excitation at 808 nm. Thus, the presence of emission bands between 980 and 1400 nm (biological windows II-III) was observed, where there is a high penetrability of radiation by biological tissues. Studies of UC processes after excitation with low energy radiation confirm an efficient radiation emission in the UV-vis-NIR-I region both in powder and in aqueous dispersion samples. At 980 nm, Yb^{3+} ions have been described to act as sensitizing ions, and Nd^{3+} and Tm^{3+} ions as activators, while at 808 nm the energy transfer mechanism involves Yb^{3+} ions acting as bridging ions transferring energy in the direction: $Nd^{3+}\rightarrow Yb^{3+}\rightarrow Tm^{3+}$. As a result of all these studies, it is concluded that $Y_{0.9}Nd_{0.02}Tm_{0.03}Yb_{0.05}VO_4$-HT-MA sample has turned out to be the most promising for future optical applications. As a future direction, we aim to evaluate this sample as a fluorescent probe for *in vivo* cancer cell assays.

CRediT authorship contribution statement

María Rapp: Writing – original draft, Software, Methodology, Investigation, Data curation. **Elisa Ortiz-Rivero:** Validation, Software, Methodology, Investigation, Data curation. **Josefa Isasi:** Writing – review & editing, Validation, Supervision, Project administration, Funding acquisition. **Mauricio Alcolea Palafox:** Writing – review & editing, Validation, Project administration, Funding acquisition.

Data availability

The raw/processed data required to reproduce these findings cannot be shared at this time due to technical or time limitation.

Declaration of competing interest

The authors declare that they have no known competing financial interests or personal relationships that could have appeared to influence the work reported in this paper.

Acknowledgements

This work was financially supported by the Spanish Ministry of Science and Innovation, through projects PID2019-106211RB-I00, and PID2019-105195RA-I00, the Instituto de Salud Carlos III (PI16/00812) and (PI19/00565), by the Comunidad Autónoma de Madrid (B2017/BMD-3867RENIMCM) and by Universidad Autónoma de Madrid and Comunidad Autónoma de Madrid (SI1/PJI/2019-00052). E.O.R gratefully acknowledges the financial support provided by the Spanish Ministerio de Universidades, through the FPU program (FPU19/04803) and the Ramón Areces Foundation for a postdoctoral fellowship.

Appendix A. Supplementary data

Supplementary data to this article can be found online at https://doi.org/10.1016/j.ceramint.2025.01.583.

References

[1] A. Skripka, R. Marin, A. Benayas, P. Canton, E. Hemmer, F. Vetrone, Covering the optical spectrum through collective rare-earth doping of $NaGdF_4$ nanoparticles: 806 and 980 nm excitation routes, Phys. Chem. Chem. Phys. 19 (19) (2017) 11825–11834, https://doi.org/10.1039/c7cp01167a.

[2] B. Zhou, S. Liu, Q. Zhang, Tuning and optimization of upconversion phosphors, in: Upconversion Nanophosphors, Elsevier, 2021, pp. 251–290, https://doi.org/10.1016/B978-0-12-822842-5.00010-8.

[3] B. Klimesz, R. Lisiecki, W. Ryba-Romanowski, Thermosensitive Tm^{3+}/Yb^{3+} co-doped oxyfluorotellurite glasses – spectroscopic and temperature sensor properties, J. Alloys Compd. 823 (May 2020) 153753, https://doi.org/10.1016/J.JALLCOM.2020.153753.

[4] M. Rapp, J. Isasi, M. Alcolea Palafox, T. Muñoz-Ortiz, E. Ortiz-Rivero, Synthesis, structural and morphological characterization and photoluminescence study of $Y_{0.9}Er_{0.1-x}Yb_xVO_4$ materials, J. Alloys Compd. 903 (May 2022) 163930, https://doi.org/10.1016/J.JALLCOM.2022.163930.

[5] Y. Lozano, et al., Synthesis of new non-covered and silica-covered $Y_{0.9}Tm_{0.1-x}Yb_xVO_4$ nanophosphors with emission in the visible and NIR ranges, J. Lumin. 257 (May 2023) 119708, https://doi.org/10.1016/J.JLUMIN.2023.119708.

[6] S.T. Dibaba, Xiaoqian Ge, W. Ren, L. Sun, Recent progress of energy transfer and luminescence intensity boosting mechanism in Nd^{3+}-sensitized upconversion nanoparticles, J. Rare Earths 37 (8) (Aug. 2019) 791–805, https://doi.org/10.1016/J.JRE.2019.02.001.

[7] Y. Tian, et al., Laser-induced thermal effect and the role of Nd^{3+} in $Tm^{3+}/Yb^{3+}/Nd^{3+}$ triply doped $LaNbO_4$ up-conversion phosphors under 808 nm excitation, J. Lumin. 223 (Jul. 2020) 117201, https://doi.org/10.1016/J.JLUMIN.2020.117201.

[8] A. Skripka, et al., Decoupling theranostics with rare earth doped nanoparticles, Adv. Funct. Mater. 29 (12) (Mar. 2019), https://doi.org/10.1002/adfm.201807105.

[9] Y.F. Wang, G.Y. Liu, L.D. Sun, J.W. Xiao, J.C. Zhou, C.H. Yan, Nd3+-sensitized upconversion nanophosphors: efficient in vivo bioimaging probes with minimized heating effect, ACS Nano 7 (8) (Aug. 2013) 7200–7206, https://doi.org/10.1021/nn402601d.

[10] S. Ray, A. Banerjee, P. Pramanik, A novel rock-like nanoarchitecture of $YVO_4:Eu^{3+}$ phosphor: selective synthesis, characterization, and luminescence behavior, J. Mater. Sci. 45 (1) (Jan. 2010) 259–267, https://doi.org/10.1007/s10853-009-3928-3.

[11] H. Li, N. Luo, D. Luo, L. Xiong, L. Yang, M. Zhao, Effect of calcination temperature on the microstructure and optical properties of monodispersed self-assembled yttrium orthovanadate microspheres, J. Lumin. 234 (Jun. 2021) 117990, https://doi.org/10.1016/J.JLUMIN.2021.117990.

[12] M.J. Mitchell, M.M. Billingsley, R.M. Haley, M.E. Wechsler, N.A. Peppas, R. Langer, Engineering precision nanoparticles for drug delivery, Nat. Rev. Drug Discov. 20 (2) (2021) 101–124, https://doi.org/10.1038/s41573-020-0090-8.

[13] L. Alcaraz, J. Isasi, Synthesis and study of Y0.9Ln0.1VO4 nanophosphors and $Y_{0.9}Ln_{0.1}VO_4@SiO_2$ luminescent nanocomposites with Ln=Eu, Dy, Er, Ceram. Int. 43 (6) (Apr. 2017) 5311–5318, https://doi.org/10.1016/J.CERAMINT.2017.01.069.

[14] M. Fernández-Ramos, J. Isasi, M. Alcolea, T. Muñoz-Ortiz, E. Ortiz-Rivero, New magnetic-fluorescent bifuntional $(Y_{0.9}Ln_{0.1}VO_4/Fe_3O_4)@SiO_2$ and $[(Y_{0.9}Ln_{0.1}VO_4@SiO_2)/Fe_3O_4@SiO_2]$ materials, Ceram. Int. 48 (15) (Aug. 2022) 22006–22017, https://doi.org/10.1016/J.CERAMINT.2022.04.191.

[15] Y. Liang, J. Ouyang, H. Wang, W. Wang, P. Chui, K. Sun, Synthesis and characterization of core–shell structured $SiO_2@YVO_4:Yb^{3+}$, Er^{3+} microspheres, Appl. Surf. Sci. 258 (8) (Feb. 2012) 3689–3694, https://doi.org/10.1016/J.APSUSC.2011.12.006.

[16] I.E. Kolesnikov, E.V. Golyeva, M.A. Kurochkin, E. Lähderanta, M.D. Mikhailov, Nd^{3+}-doped YVO_4 nanoparticles for luminescence nanothermometry in the first and second biological windows, Sensor. Actuator. B Chem. 235 (Nov. 2016) 287–293, https://doi.org/10.1016/j.snb.2016.05.095.

[17] E.V. Golyeva, D.V. Tolstikova, I.E. Kolesnikov, M.D. Mikhailov, Effect of synthesis conditions and surrounding medium on luminescence properties of $YVO_4:Eu^{3+}$ nanopowders, J. Rare Earths 33 (2) (Feb. 2015) 129–134, https://doi.org/10.1016/S1002-0721(14)60392-6.

[18] L. Dimesso, Pechini processes: an alternate approach of the sol-gel method, preparation, properties, and applications, in: Handbook of Sol-Gel Science and Technology: Processing, Characterization and Applications, Springer International Publishing, 2018, pp. 1067–1087, https://doi.org/10.1007/978-3-319-32101-1_123.

[19] P.P. Ghimire, M. Jaroniec, Renaissance of Stöber method for synthesis of colloidal particles: new developments and opportunities, J. Colloid Interface Sci. 584 (Feb. 2021) 838–865, https://doi.org/10.1016/J.JCIS.2020.10.014.

[20] C. Ferrer, et al., Structural and magnetic studies of $NiFe_2O_4$ and $NiFe_2O_4@SiO_2$-Silane agent samples useful for the removal of Cu^{2+} ions, J. Alloys Compd. 899 (2021) 163403, https://doi.org/10.1016/j.jallcom.2021.163403.

[21] R.D. Shannon, Revised effective ionic radii and systematic studies of interatomie distances in halides and chaleogenides, Found. Crystallogr. 32 (5) (1976) 751–767, https://doi.org/10.1107/S0567739476001551.

[22] L. Alcaraz, J. Isasi, Influence of the synthesis conditions of $Y_{0.9}Dy_{0.1}VO_4$ on the powder morphology and luminescence emission intensity, J. Nanoparticle Res. 21 (2019) 1–13, https://doi.org/10.1007/s11051-019-4514-5.

[23] Y. Liang, J. Ouyang, H. Wang, W. Wang, P. Chui, K. Sun, Synthesis and characterization of core-shell structured $SiO_2@YVO_4:Yb^{3+}$,Er^{3+} microspheres,

Appl. Surf. Sci. 258 (8) (Feb. 2012) 3689–3694, https://doi.org/10.1016/j.apsusc.2011.12.006.

[24] M.S. Beg, J. Mohapatra, L. Pradhan, D. Patkar, D. Bahadur, Porous Fe_3O_4-SiO_2 core-shell nanorods as high-performance MRI contrast agent and drug delivery vehicle, J. Magn. Magn Mater. 428 (Apr. 2017) 340–347, https://doi.org/10.1016/j.jmmm.2016.12.079.

[25] X. Zhang, et al., Magnetic and optical properties of $NaGdF_4$:Nd^{3+}, Yb^{3+}, Tm^{3+} nanocrystals with upconversion/downconversion luminescence from visible to the near-infrared second window, Nano Res. 8 (2) (Feb. 2015) 636–648, https://doi.org/10.1007/s12274-014-0548-2.

[26] M. Gunaseelan, S. Yamini, G.A. Kumar, D.K. Sardar, J. Senthilselvan, Reverse microemulsion synthesis of mixed α and β phase $NaYF_4$:Yb,Er nanoparticles: calcination induced phase formation, morphology, and upconversion emission, J. Sol. Gel Sci. Technol. 96 (3) (Dec. 2020) 550–563, https://doi.org/10.1007/s10971-020-05340-w.

[27] T. Grzyb, P. Kamiński, D. Przybylska, A. Tymiński, F. Sanz-Rodríguez, P. Haro Gonzalez, Manipulation of up-conversion emission in $NaYF_4$core@shell nanoparticles doped by Er^{3+}, Tm^{3+}, or Yb^{3+}ions by excitation wavelength-three ions-plenty of possibilities, Nanoscale 13 (15) (Apr. 2021) 7322–7333, https://doi.org/10.1039/d0nr07136f.

[28] J. Shen, et al., Engineering the upconversion nanoparticle excitation wavelength: cascade sensitization of tri-doped upconversion colloidal nanoparticles at 800 nm, Adv. Opt. Mater. 1 (9) (Sep. 2013) 644–650, https://doi.org/10.1002/adom.201300160.

[29] B. Xu, et al., Tunable emission and color temperature of Yb^{3+}/Er^{3+}/Tm^{3+}-tridoped Y_2O_3-ZnO ceramic nano-phosphors using Er^{3+} concentration and excitation pump power, Nanomaterials 12 (12) (Jun. 2022), https://doi.org/10.3390/nano12122107.

[30] A. Skripka, et al., Decoupling theranostics with rare earth doped nanoparticles, Adv. Funct. Mater. 29 (12) (Mar. 2019), https://doi.org/10.1002/adfm.201807105.

[31] Y. Zhang, et al., Concentration quenching of blue upconversion luminescence in Tm^{3+}/Yb^{3+} co-doped $Gd_2(WO_4)_3$ phosphors under 980 and 808 nm excitation, J. Alloys Compd. 709 (Jun. 2017) 147–157, https://doi.org/10.1016/J.JALLCOM.2017.03.125.

[32] X. Yinsheng, et al., Bright red upconversion luminescence of thulium ion-doped GeS_2−In_2S_3−CsI glasses, J. Phys. Chem. C 113 (22) (Jun. 2009) 9911–9915, https://doi.org/10.1021/jp9010857.

[33] S. Karmegam, M. Kolikkaje, S.D. George, Solvent-dependent upconversion luminescent studies of single and colloidal nanoparticles, J. Phys. Chem. C 128 (35) (Sep. 2024) 14709–14716, https://doi.org/10.1021/acs.jpcc.4c02521.

[34] H. Ling, et al., Effect of surface modification on the luminescence of individual upconversion nanoparticles, Small 20 (26) (Jun. 2024), https://doi.org/10.1002/smll.202309035.